Manipulating dielectric relaxation via anisotropic field deviations in perovskite titanate grain–grain boundary heterostructure: a joint experimental and theoretical venture

Souvik Bhattacharjee[1] · Ratna Sarkar[1] · Pratik Chattopadhyay[2] · Anibrata Banerjee[2] · Nirmalya Sankar Das[3] · Dimitra Das[2] · Kalyan Kumar Chattopadhyay[1,2]

Abstract

Effect of dc field is comprehended in impedance, dielectric, admittance and modulus spectra (40 Hz–20 MHz) of solid-state synthesized, polycrystalline calcium, strontium and barium titanate nanoparticles. The phase conformation, stoichiometry, optical and vibrational characteristics are investigated employing XRD-Rietveld analysis, DRS, FTIR and Raman spectra. The real/imaginary parts of impedance, dielectric and related functions are tailored by varying external field in the context of classical energy-storing bottleneck. The field-dependent Nyquist plots are interpreted from a proposed equivalent circuitry to quantify electrically heterogeneous, grain core–grain boundary (GC–GB) resistance correlations. Relaxation times, shape parameters and low/high-frequency limits are tailored following Cole–Davidson and Johnson's equations, that explicate Maxwell–Wagner interfacial polarization (MWIP). Using the modified Kohlrausch–Williams–Watts (KWW) equation, asymmetric broadening in modulus spectra is analyzed to attune the non-Debye relaxations, free from electrode effects. Large polaron hopping conduction is scrutinized using Jonscher's power law to emphasize variable-range and correlated-barrier hopping mechanisms, comprising delocalized/de-trapped carriers. Bias insurgence promotes Debye relaxations, which however suspends switching of the fundamental relaxation channel, leading to a single normalized master modulus curve. Static dielectric tensors, Born effective charges and field-induced charge cloud separation are enunciated via density functional theory (DFT) framework, whereas finite element simulations using experimentally extracted electrical parameters substantiate non-uniform and anisotropic field-diffusion within the GC–GB heterostructure.

Graphical abstract
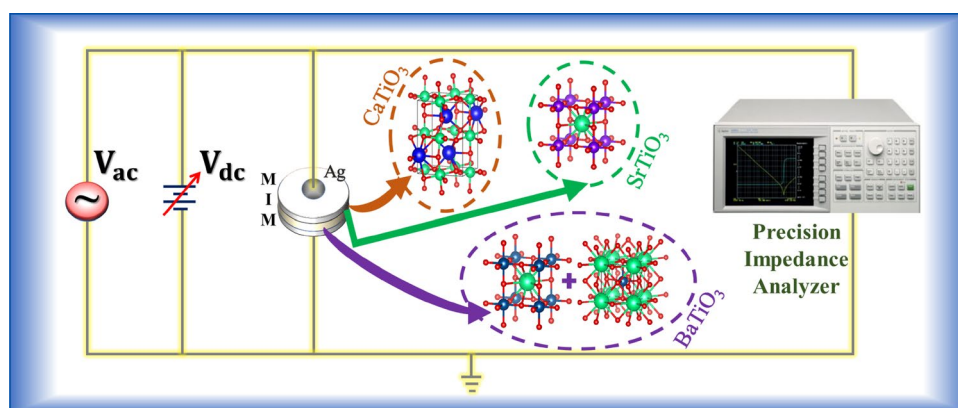
Keywords $ATiO_3$ nanoparticles · Non-Debye relaxations · Polaron hopping · Field-dependent properties · Density functional theory · Finite element simulations

1 Introduction

The emerging thrust for lead-free nanomaterials that offer an extensive variety of coexisting dielectric, piezoelectric and (relaxor or normal) ferroelectric properties along with thermal and compositional stability have promoted a plethora of investigations on alkaline-earth perovskite titanates (ATiO$_3$; A = Ca, Sr, Ba; respectively abbreviated as CT, ST and BT henceforth) and its composites or superlattices [1–9]. This garnered diverse strategies and desirable applications as electro-ceramic and inexpensive microelectronic devices viz., multi-layered energy-storing or -coupling capacitors, pyroelectric detectors, high density optical memory and radar devices, thermistors with positive temperature coefficients, bandpass filters for broadcasting and telecommunications, superior ultrasonic transducers and actuators, etc. [9–15]. The use of ultrafine grains of dielectric compounds like titanates not only improves energy density, breakdown strength and response time, but also advances miniaturized and portable electronic devices [2, 9, 16, 17]. Apart from primary electronics, these groups of materials are promising in design and development of water splitting photo-electrodes, nanophosphors (via quenching polar discontinuities), electro-catalyst and gas sensors as well, which again requires intriguing dielectric properties, tunability of conductivity bottleneck (especially photo-generated carriers and their recombination mechanism) and electro-optic coefficient [17–21].

Among these three compounds, CT and ST are known to be quantum paraelectric materials [1, 6, 8]. The suppression of long-range ferroelectric order by quantum fluctuations accounts for the quantum paraelectric phase. Both these compounds offer to have large dielectric constant due to softening of long wavelength transverse optic phonon modes [6]. But, the difference in their dielectric permittivity is due to the tilted [TiO$_6$] octahedra, which prevents long-range coupling between neighboring unit cells [4–8]. BT, which is the first perovskite-type ferroelectric discovered and studied since late 1940s, has four recognized crystal structures over a broad temperature range viz., rhombohedral, orthorhombic, tetragonal and cubic (such phases exist for CT and ST also at cryogenic temperatures) [6–9]. The first three phases are ferroelectric with polarizations along [110], [111] and [100] direction respectively caused by an acute off-centering of the Ti^{4+} ions from the [TiO$_6$] octahedra, while the cubic phase is paraelectric. In the ideal cubic structure of perovskites, B (typically transition metal) ions lie at the center of the O-octahedra and oxygen atoms are placed at the face centers, while the A cations rest at the larger 12-fold coordinated sites. Such an ideal structure assimilates various structural instabilities that involve displacement of the cations to non-centrosymmetric positions as well as rotations and (Jahn–Teller) distortion of the O-octahedra [20–23]. The interplay of particular instabilities and disorders foster transformation to lower symmetries and establish the rich variety in (anti)ferroelectrics and multiferroics. In this regard, Sai et al. conducted first principles studies on cubic perovskites of the form $\left(A_{1/3}A'_{1/3}A''_{1/3}\right)BO_3$ and $A\left(B_{1/3}B'_{1/3}B''_{1/3}\right)O_3$ with alternate series of monolayers having distinct cations [22]. They reported a strong variation in the strength of symmetry breaking with associated compositional perturbation, building a proficient ferroelectric nature. Liu et al. plumped for epitaxial $(Ba, Sr)TiO_3//Ba(Zr, Ti)O_3$ heterostructures doped with Mn to enhance dielectric constant and ferroelectric polarization with controlled dissipation, by optimizing thickness-ratios of deposited layers and sequencing [23]. Similar enhancements are also analyzed using DFT-based approaches to confirm the effect of lattice strains, anisotropy and distortions [24].

Dielectric spectroscopy archetypically concentrates at recognizing the very nature and origin of polarization, such as relaxation (e.g., orientational, interfacial) or deformational component (e.g., ionic, electronic) of polarizability, to understand the electrical microstructure in a heterogeneous system. Basically, the accumulated charge at the interface between the grain core and boundary and an internal barrier layer capacitance (IBLC) establishes Maxwell–Wagner interfacial polarization (MWIP) [7–9, 23, 25]. Consequently, Raevski et al. suggested an effective dielectric constant of the core–shell structure: $\varepsilon' = \varepsilon'_{gb}\left(t_g + t_{gb}\right)/t_{gb}$ at the low-frequency regime, where ε'_{gb} is the contribution of the grain boundary (shell) and t_g and t_{gb} are the thickness of the respective parts [26]. Currently, tailoring dielectric constant, loss and conductivity are the central goals in this field and substitutional doping is the most common method for accomplishing that [3–5, 25, 27]. But it does not only manipulate dipolar strength or carrier density, but also end up with increased defect density, unwanted traps or elevated local strain. Effect of grain size, stress, A–B site stoichiometry/occupancy, humidity, calcination temperature, chemical and micro-structural variations are studied too in this regard [9, 16, 17, 27–30]. But, enabling reversible tunability via external parameters, such as pressure, temperature, electric or magnetic field, is preferable for commercial or industrial use. Exerting large pressure might cause expansion of defects and stress throughout the system, and can even ensue irreversible damage [28]. Also, for most piezo-ceramics, magnetodielectric effect is feeble and infrequent at room temperature. Although pyroelectricity and other temperature-dependent alterations hardly affect room temperature performance, they are fundamentally appealing for exploring materials physics. That is why, in the past few decades, immense research

already transpired pledging Arrhenius equation, Vogel–Fulcher relation and thermally activated carrier hopping in $ATiO_3$ [3–5, 8, 9, 18, 22–25, 29, 31]. Wang et al. executed comparative temperature-dependent dielectric studies in ceramic and single crystalline ST samples and observed Debye-type and relaxor-like behavior, respectively [18]. They also correlated the multi-relaxation mechanism with the formation and dissociation of single or doubly charged oxygen vacancy clusters. Contrastingly, field-dependent response is quite uniform and easy to operate in electrical or electronic gadgets. It helps to identify the underlying mechanisms, incommensurate molecular dipoles and non-Debye relaxations conclusively [30–35]. Ang et al. investigated 'field-induced ferroelectricity' and relevant couplings with soft phonon modes in some quantum paraelectric single crystal and thin films [33, 34]. They in fact inferred that the Landau–Ginzburg–Devonshire (LGD) theory cannot entirely explain the properties of many polar dielectrics and thus introduced a multi-polarization mechanism, taking both extrinsic and intrinsic contributions into account. However, the effect of dc field in various dielectric parameters is still not rigorously explored for polycrystalline perovskites. Scientific literature comprises contradicting reports on modulation of dielectric constant as a function of bias [30–36]. Moreover, nanoparticles can grasp a stronger surface polarization than their bulk counterparts because of the rise in surface-to-volume ratio of the grains, and thereby scavenge larger dielectric constant [9, 30]. Thus, a comprehensive and comparative study of bias field-dependent impedance, dielectric, admittance and modulus spectra of the $ATiO_3$ family having nano-dimension is required, which is the main objective of this work.

2 Methodology

2.1 Precursors and materials

Analytical-grade reagents (> 99.9% purity) were used without further purification. The raw ingredients: calcium carbonate ($CaCO_3$), strontium carbonate ($SrCO_3$), barium carbonate ($BaCO_3$) and titanium dioxide (TiO_2) powder were purchased from SIGMA-ALDRICH.

2.2 Synthetic procedure

Conventional solid-state method in open air was adopted to synthesize $ATiO_3$ nanoparticles. The alkaline-earth carbonates and TiO_2 powder were mixed in stoichiometric ratio and grounded thoroughly in an agate mortar for an hour to obtain homogeneous fine particles. Then the mixture was taken in an alumina crucible and calcined in a high temperature muffle furnace. In the decarbonation step, the temperature

was elevated systematically to 600 °C (2 h), 800 °C (2 h) and 1000 °C (10 h). Accompanying periodic grindings, the mixture of oxides was finally sintered at 1275 °C for 6 h to obtain $ATiO_3$ phase. The average ramp-up rate was maintained at 4 °C/min, while the cooling was set to be natural. The associated reactions follow:

$$ACO_3 \xrightarrow{1000\ °C} AO + CO_2$$

$$AO + TiO_2 \xrightarrow{1275\ °C} ATiO_3$$
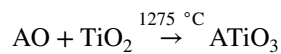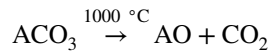
Although most experiments can be performed with the as-obtained nano-powder, dielectric characterizations manifest the best data (with low leakage conductance and associated noise) with MIM pellets. So, 0.40 g of each sample is uniaxially cold-pressed at 0.6 GPa pressure using a hydraulic press to produce polycrystalline cylindrical pellets of 9.5 mm diameter and 1.1 mm thickness. To truncate cracks, enhance compressive strength and density, they were further calcined at 1275 °C for an hour. The calculated densities of CT, ST and BT pellets are 3.92, 4.76 and 5.95 g cm^{-3}, respectively, which are very close to their standard densities. For electrical characterizations, thin copper wires were connected to the opposite faces of the pellets using silver paint (Alfa Aesar) to uphold MIM configuration. Formation of non-rectifying, ohmic contacts is anticipated because of (a) high electrical conductivity of silver, (b) closeness of electron affinity of the titanates to the work function of silver, and (c) smaller interface barrier.

2.3 Experimental methods and instrumental specifications

Please visit the Supplementary Information (SI).

2.4 Computational details for DFT-based calculations

Please visit the SI.

2.5 Finite element electrostatic simulations (FEES)

FEES were further conducted using the ANSYS Maxwell software to demonstrate the anisotropic build-up of electric field/flux in the GC–GB heterostructure. A miniaturized 3D model of $4 \times 4 \times 3$ semiconducting nano-cores dispersed in the grain boundary host is thus constructed and sandwiched between silver electrodes, implementing experimentally extracted electrical parameters to physically decipher the effect of unidirectional field on the nanoscopic architecture of the compounds. The dimensions are adapted as per the

actual capacitive assembly in accordance to the FESEM micrographs.

3 Results and discussion

3.1 X-ray diffraction and Rietveld analysis

All Bragg peaks obtained in the XRD patterns (Fig. 1) of the respective samples are matched with ICSD PDF cards: 01–088-0790 (CT, orthorhombic, *Pbnm*), 01–073-0661 (ST, cubic, *Pm$\bar{3}$m*), and 01–079-2263 (BT, cubic, *Pm$\bar{3}$m*), respectively. From calcium to barium compound, shift of the most intense peak to a smaller angle can be detected clearly, that suggests a gradually expanding interplanar spacing. Absence of additional peaks or deviations in the first two samples (CT and ST) confirm purity of phase. However, for BT nanoparticles, implications of a secondary tetragonal phase (*P4mm*) are found. It is well known that, for ceramic BT samples having μm-order dimension, purely tetragonal (ferroelectric) structure survives. But,

for nanoparticles, the cubic (paraelectric) phase becomes thermodynamically more stable, which may stimulate formation of mixed phase [16].

The corresponding crystallite sizes $\left(D_{cryst}\right)$ are determined from the Scherrer's equation:

$$D_{cryst} = \frac{K\lambda}{\beta \cos\theta} \cong \frac{0.89\lambda}{\beta \cos\theta}. \tag{1}$$

Here K is a dimensionless constant, that depends on the geometry or shape of the particles, λ is the wavelength of the incident X-ray (= 1.5406 Å), and β represents the FWHM of the Bragg peaks. Based on the five most intense peaks, mean crystallite sizes are calculated to be 43.5, 59.2 and 48.1 nm for the respective samples. The FESEM micrographs are shown in Fig. S2, that exhibit quite larger particles of grain size: 80–100 nm, compared to the crystallite sizes, suggesting a polycrystalline growth. The nanoparticles develop a near-spherical morphology with moderate agglomeration as a result of high temperature sintering. The agglomeration increases more after palletization.

Starting from the standard crystallographic information files (CIFs), the crystalline structures are refined according to the Rietveld's method deploying the FULLPROF software. A pseudo-Voigt line-profile function is considered to compute lattice parameters, scale factor, micro-strain, atomic positions, occupancy, isotropic thermal parameters, etc., see Fig. 1 and Table 1. Results for CT, ST and BT nanoparticles are provided in Fig. 1a–c. Observed diffraction traces are shown by open blue circles, while the refined pattern is indicated by the pink curve. The green vertical bars show the positions of corresponding Bragg peaks and the maroon line represents the difference between the observed and calculated intensities i.e., $\left(I_{obs} - I_{calc}\right)$. Nominal internal strain in all three samples is noted, that accords use of Scherrer's formula. The consolidated parameters provided in Table 1 testify fine crystallinity and stoichiometry for all three samples, against a competent (< 2) goodness-of-fit: $\chi^2 = \left(R_{wp}/R_{exp}\right)^2$, where R_{wp} and R_{exp} are the weighted and expected profile residual factors. The quality of refinement can be verified from the following values viz., CT: $R_{wp} = 3.51\%, R_{exp} = 3.43\%, \chi^2 = 1.05$; ST: $R_{wp} = 4.32\%, R_{exp} = 3.07\%, \chi^2 = 1.98$; BT: $R_{wp} = 3.97\%, R_{exp} = 2.89\%, \chi^2 = 1.89$. Although CT is purely orthorhombic and ST is purely cubic, the crystalline conformation in BT indicates a 68 : 32 phase ratio between cubic and tetragonal growth. The as-refined unit cells of the three compounds (including a mixed phase) are extracted from FULLPROF program and processed in the VESTA software to display the final crystal structures, see Fig. 2.
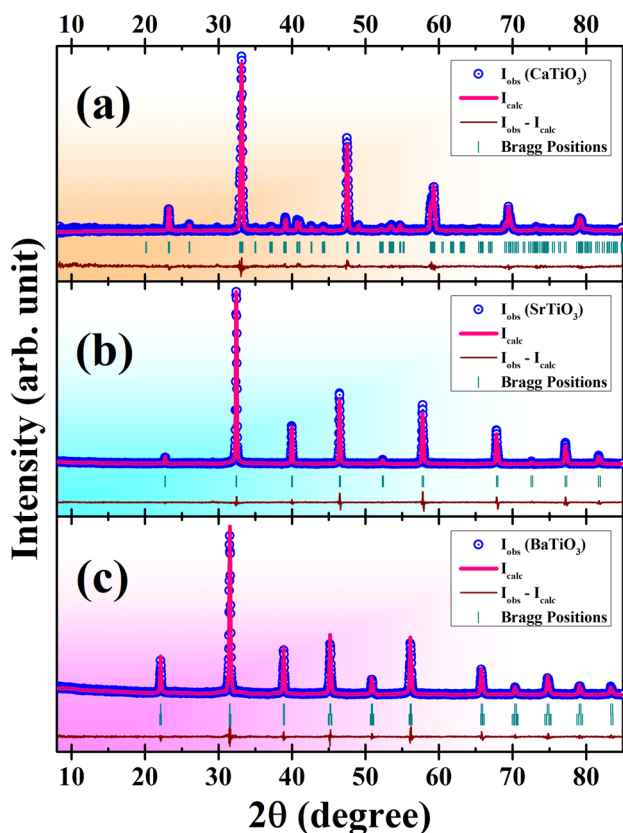

Fig. 1 Observed (open blue circles) and refined (pink curve) powder XRD pattern for **a** CT, **b** ST and **c** BT nanoparticles. The green vertical bars represent corresponding Bragg peaks and the maroon line indicates the difference of the experimental diffraction traces to the calculated best fit

Table 1 Rietveld analysis of XRD data: refined crystallographic parameters

Sample (space group)	Lattice parameters*	Strain (η %)	Atoms	Wyckoff sites	x	y	z	Occupancy	χ^2
$CaTiO_3$ (Pbnm)	a = 5.3866(7) Å; b = 5.4421(9) Å; c = 7.6453(6) Å; V = 224.125(9) Å	0.46	Ca	4c	− 0.00910	0.03393	0.25000	0.500	1.05
			Ti	4b	0.00000	0.50000	0.00000	0.500	
			O1	4c	0.07108	0.47848	0.25000	0.500	
			O2	8d	0.70911	0.28952	0.03700	1.000	
$SrTiO_3$ ($Pm\bar{3}m$)	a = b = c = 3.9067(0) Å; V = 59.625(2) Å³	0.63	Sr	1b	0.50000	0.50000	0.50000	1.000	1.98
			Ti	1a	0.00000	0.00000	0.00000	0.977	
			O	3d	0.50000	0.00000	0.00000	1.049	
$BaTiO_3$ ($Pm\bar{3}m$) [~ 68%]	a = b = c = 4.0130(7) Å; V = 64.249(4) Å	0.19	Ba	1b	0.50000	0.50000	0.50000	1.000	1.89
			Ti	1a	0.00000	0.00000	0.00000	0.974	
			O	3d	0.50000	0.00000	0.00000	1.073	
$BaTiO_3$ (P4mm) [~ 32%]	a = b = 3.9999(0) Å; c = 4.0170(0) Å; V = 64.268(8) Å	0.15	Ba	1a	0.00000	0.00000	0.00000	0.961	
			Ti	1b	0.50000	0.50000	0.58388	1.409	
			O1	1b	0.50000	0.50000	0.06857	1.416	
			O2	2c	0.50000	0.00000	0.58299	1.928	

*For all the crystal systems under consideration, $\alpha = \beta = \gamma = 90°$ is applicable

(a) Orthorhombic $CaTiO_3$ (Pbnm)　**(b) Cubic $SrTiO_3$ ($Pm\bar{3}m$)**　**(c) Cubic $BaTiO_3$ ($Pm\bar{3}m$)**　**(d) Tetragonal $BaTiO_3$ (P4mm)**
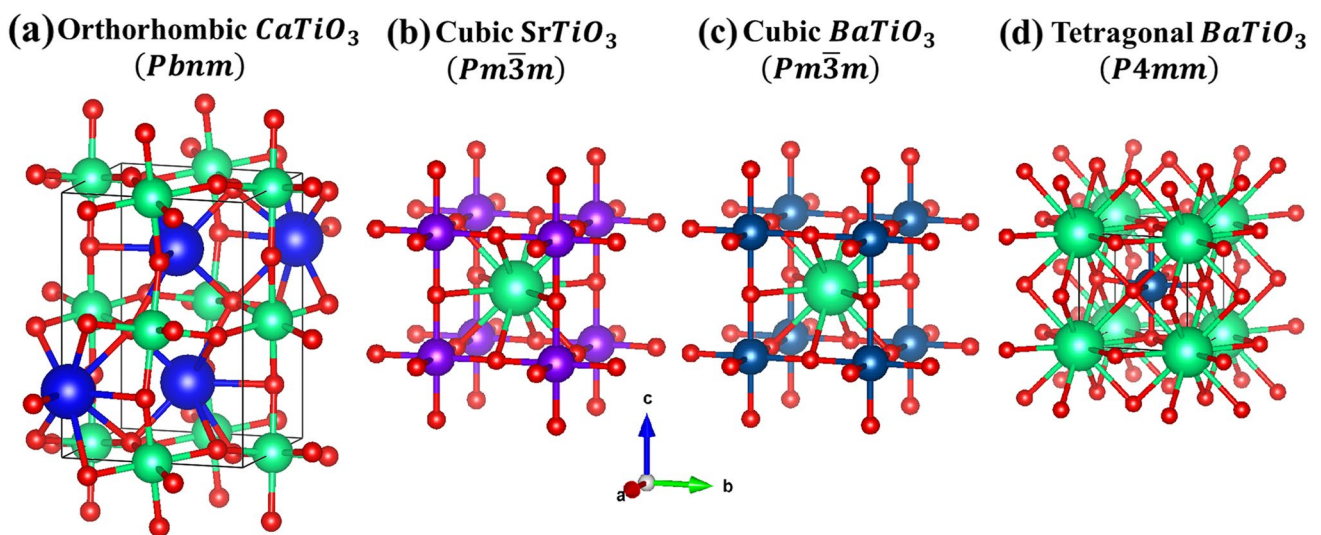
Fig. 2 Refined crystal structure of the as-obtained phases: unit cells of **a** orthorhombic CT; **b** cubic ST; **c** cubic BT and **d** tetragonal BT. The red, green and different shades of blue-colored balls represent oxygen, titanium and alkaline-earth metal atoms, respectively

Table 2 Elemental weight and atomic proportions determined from the EDX spectra

Elements	$CaTiO_3$		$SrTiO_3$		$BaTiO_3$	
	Wt (%)	Atom (%)	Wt (%)	Atom (%)	Wt (%)	Atom (%)
A (Ca/Sr/Ba)	31.21	21.20	48.19	20.25	55.82	18.02
Ti	33.77	19.20	25.78	19.83	21.91	20.29
O	35.02	59.60	26.03	59.92	22.27	61.69

3.2 Stoichiometric assessment from energy-dispersive X-ray (EDX) spectra

EDX spectra were acquired for the perovskite nanoparticles (check Fig. S3), that demonstrate clear peaks of no elements other than the alkaline earths, titanium and oxygen. The peaks of the cations are closely spaced, but easy to resolve. To verify the elemental stoichiometry of the samples, weight and atomic %ages are determined from the spectra and provided in Table 2. For all three compounds, the atomic ratio is very close to 1 : 1 : 3, which confirms the composition.

3.3 DRS and bandgap evaluation

All three samples attain low reflectance and therefore strong absorption characteristics over $200 - 400$ nm incident radiation (UV), see Fig. 3a. For longer wavelengths, they reflect a vast majority of the incident intensity consistently, that indicates a wide gap band structure. Conventionally the allowed, direct optical bandgap $\left(E_g\right)$ is calculated from the Tauc's equation:

$$(\alpha h\nu)^2 = A_0\left(h\nu - E_g\right). \tag{2}$$

Here, h is the Planck's constant, ν is the excitation frequency and A_0 is the band tailing parameter, related to the probability of optical transitions between particular filled and vacant states. For non-transparent samples, rather than absorption spectroscopy, the absorption coefficient (α) is estimated using the following function as per Kubelka–Munk theory:

$$F(R) = \frac{k_m}{s} = \frac{(1 - R)^2}{2R}, \tag{3}$$

where R is the diffuse reflectance, $k_m \approx (1 - R)^2$ is the molar absorption coefficient and $s \approx 2R$ is called the scattering factor. At the absorption band edge, the extrapolated $(\alpha h\nu)^2$ vs $h\nu$ straight line estimates the bandgap: $E_g = h\nu|_{\alpha=0}$, see Fig. 3b. The as-determined bandgaps for calcium, strontium and barium titanate are 3.63, 3.34 and 3.58 eV, respectively [12].
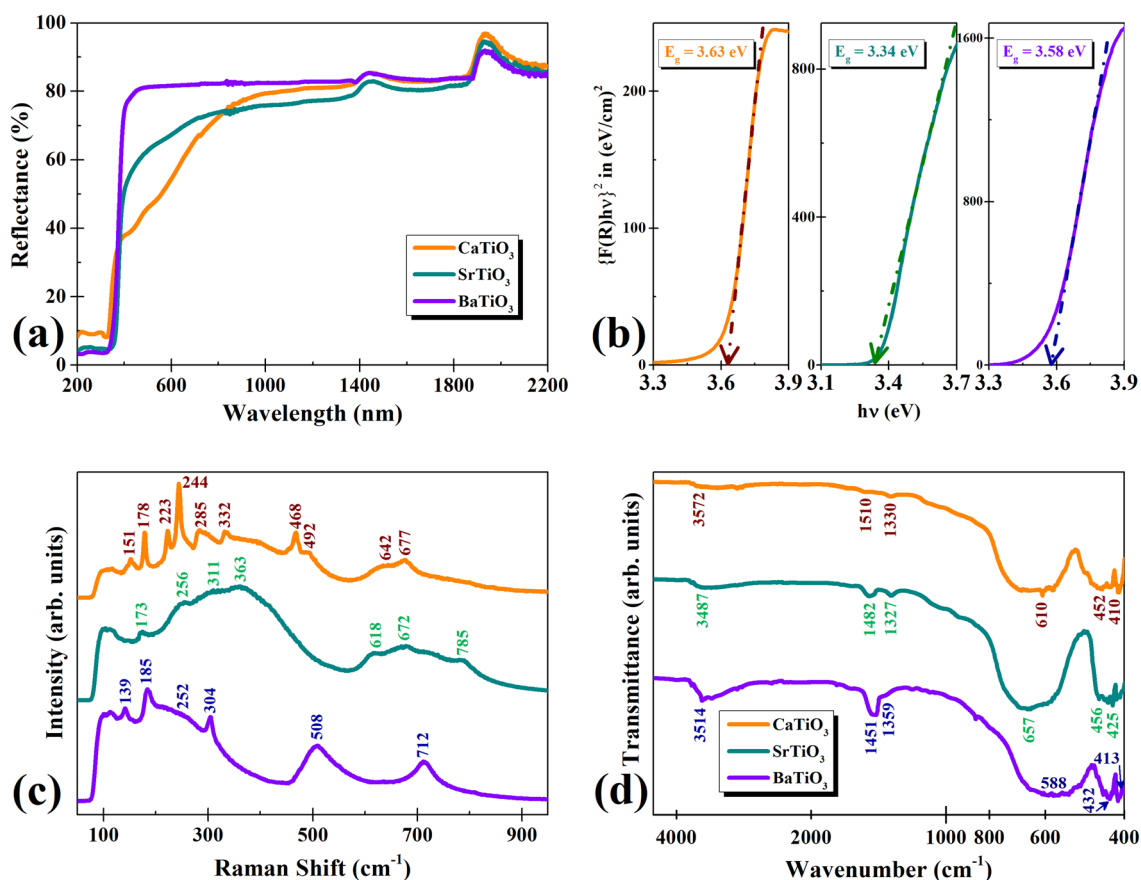

Fig. 3 **a** Diffused reflectance spectra; **b** Tauc's plots and determination of optical bandgaps $\left(E_g\right)$, employing Kubelka–Munk function $\{F(R)\}$; **c** Raman spectra and **d** FTIR transmittance spectra for CT (orange), ST (green) and BT (violet) nanoparticles

3.4 Raman and FTIR spectra: study of lattice vibrations

The finger-print modes of molecular vibration are further characterized via FTIR and Raman spectroscopy to confirm the phase coordination from phonon dynamics. Considering the refined space groups, factor group analysis is conducted using VIBRATE software as per the selection rules at the Brillouin zone center for all four phases, see SI. The irreducible modes of vibration and the IR/rotation/Raman active or optically silent modes are thereby enlisted in Table 3. The Raman modes in $ATiO_3$ perovskites often represent B site disorder and loss of translation/inversion symmetries [37].

As shown in Fig. 3c, the orthorhombic CT phase gives rise to a number of peaks at 151, 178, 223, 244, 285, 332, 468, 492, 642, and 677 cm^{-1}, that conform previous reports [6, 37]. The peaks at 151 and 178 cm^{-1} are caused by the motion of A site ions, while the peaks in the region 223–332 cm^{-1} are related to the tilting or rotations of [TiO$_6$]–[TiO$_6$] clusters. The band observed at 642 cm^{-1} is assigned to the Ti–O symmetric stretching vibration, whereas the peaks at 468 and 492 cm^{-1} are attributed to Ti–O torsional modes, associated to the bending or internal vibration of the oxygen cage. In both the cubic phases, first-order Raman scattering is completely forbidden, as mentioned in Table 3. For ST, two broad humps are recorded at 200–500 and 600–800 cm^{-1} with particular local surges [19]. They are actually indicative of second-order Raman scattering, characteristic of cubic ST phase [4]. On the other hand, for BT, the subsidiary tetragonal phase having a lower symmetry is strongly Raman active owing to critical changes in the selection rule and generates a number of Raman modes at $139(A_1), 185(E), 252(A_1), 304(E - TO_3/LO_2), 508(A_1 - TO_3) \& 712(A_1 - LO_3 + E - LO_4)$ cm^{-1} [38, 39].

FTIR spectra are displayed in Fig. 3d for all three samples, which show near-similar features [11]. Strong signatures of stretching/bending vibrations of A–O and Ti–O bonds were detected along with some minute signals that describe stretching of hydroxyl groups and H–O–H bending on account of nominally adsorbed moisture at the outer surface usual for perovskite nanoparticles. The transmittance dips are assigned in Table 4 with corresponding intensity levels.

3.5 Ab initio forecast from DFT

To demonstrate the effect of external electric field on the respective structures, the (110) Bragg plane is selected and a vacuum layer of 20 Å is inserted in the z-direction to avoid mutual interactions between the planes. A 0.5 eV/Å field is applied along the positive z-direction in the cell, *i.e.*, perpendicular to the (110) plane. The displacement of the charge cloud pertaining the unipolar field is depicted in Fig. 4. Such separated, diffused and delocalized charge cloud will produce distorted relaxation kinematics for obvious reasons, that has been investigated experimentally.

Table 3 Irreducible representations: IR/rotation/Raman active and optically silent modes for different space group or phases

	CaTiO$_3$(*Pbnm*)	SrTiO$_3$ and BaTiO$_3$ $\left(Pm\bar{3}m\right)$	BaTiO$_3$(*P4mm*)
Irreducible representations (Mulliken notation)	$\Gamma_{red} = 7A_g + 7B_{1g} + 5B_{2g} + 5B_{3g} + 8A_u + 8B_{1u} + 10B_{2u} + 10B_{3u}$	$\Gamma_{red} = 4T_{1u} + T_{2u}$	$\Gamma_{red} = 3A_1 + 3E$
IR active—acoustic modes (translations)	B_{1u}, B_{1u}, B_{3u}	T_{1u}	A_1, E
Rotations	B_{1g}, B_{2g}, B_{3g}	Nil	E
Raman active	$A_g, B_{1g}, B_{2g}, B_{3g}$	Nil	A_1, E
Optically silent modes	A_u	T_{2u}	Nil

Table 4 FTIR analysis: active modes and their assignment to particular lattice vibrations

Wavenumber (cm^{-1})			Intensity	Associated lattice vibrations
CaTiO$_3$	SrTiO$_3$	BaTiO$_3$		
410	425	413	Moderate	A–O interactions (tetrahedral for Ca and octahedral for Sr/Ba)
452	456	432	Strong	Ti–O–Ti bending in TiO$_6$ octahedron
610	657	588	Strong	Ti–O stretching inside TiO$_6$ octahedron (broad/diffused peak)
1330	1327	1359	Weak	O–H deformation in H$_2$O
1510	1482	1451	Weak	H–O–H bending of adsorbed moisture
3572	3487	3514	Weak	O–H stretching

Fig. 4 Charge density map at (110) Bragg plane of the pristine compound (left column), under 0.5 eV/Å external electric field along c-direction (middle column) and associated charge difference (right column) shown for **a** orthorhombic CT; **b** cubic ST; **c** cubic BT and **d** tetragonal BT. The yellow and cyan colors respectively indicate positive and negative charge accumulation under bias field
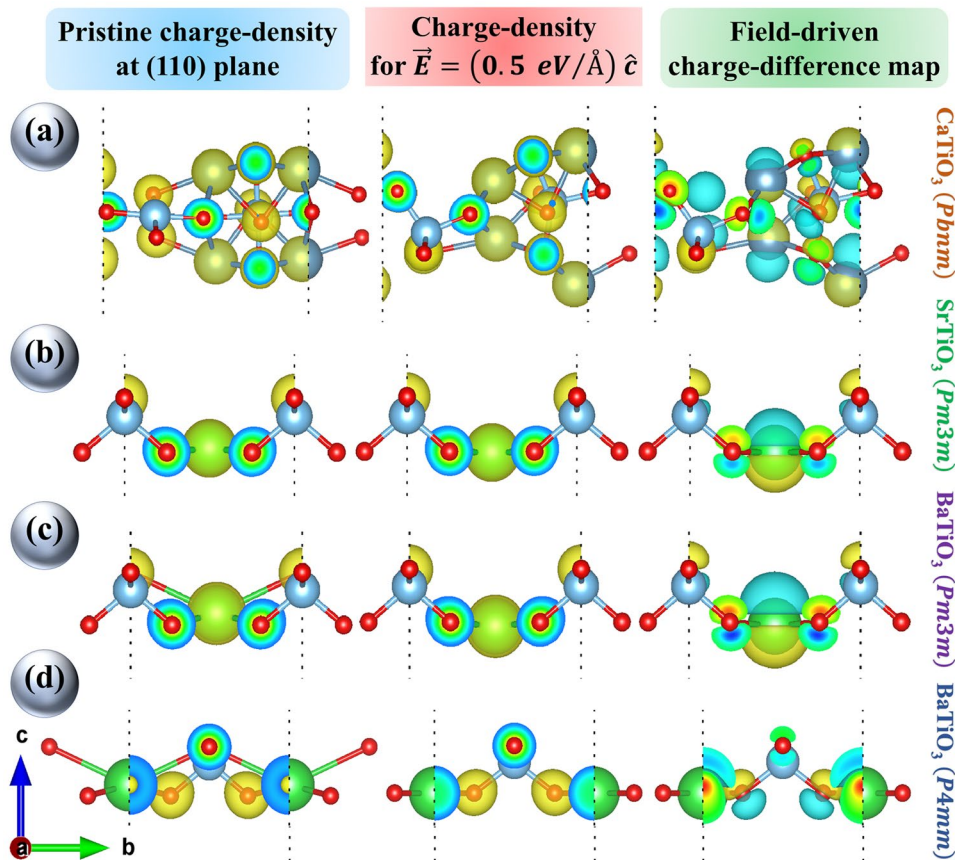
The Born effective charge (Z^*) and static dielectric tensor are computed using density functional perturbation theory (DFPT) as implemented in VASP code. The static dielectric constant $\left(\varepsilon_\infty\right)$ considering electronic contributions is found to be (i) CT: $\varepsilon_{xx} = 6.56, \varepsilon_{yy} = 6.65, \varepsilon_{zz} = 6.57$; (ii) ST: $\varepsilon_{xx} = \varepsilon_{yy} = \varepsilon_{zz} = 6.69$; (iii) BT (cubic): $\varepsilon_{xx} = \varepsilon_{yy} = \varepsilon_{zz} = 7.93$; and (iv) BT (tetrahedral): $\varepsilon_{xx} = \varepsilon_{yy} = 6.95, \varepsilon_{zz} = 6.21$, where $\forall \varepsilon_{ij} = 0$ if $i \neq j$. The Born effective charge (Z^*) relates polarization to atomic displacement, i.e., the change in polarization induced by periodic displacement in absence of external field. It is determined by the following relation:

$$Z^*_{\tau,ij} = \frac{\Omega_0}{e} \left(\frac{\delta P_i}{\delta u_{\tau,j}} \right) \Bigg|_{E=0}. \tag{4}$$

Here Ω_0 is the volume of the unit cell, δP_i is the change of polarization in the i-direction, $\delta u_{\tau,j}$ is the displacement of τth atom along the j-direction and e is the electronic charge. The calculated Born effective charge tensors for different systems are provided in the SI. Axe was first to propose an estimation of Z^* for ABO$_3$ series experimentally. It has been observed that the amplitude of Z^* deviates from static ionic charges. In our materials, Z^* of Ti and one component for

O are quite larger than their static charges (+ 4 for Ti and − 2 for O), which basically represent the mixed ionic and covalent character of the Ti–O bond.

3.6 Impedance and dielectric spectroscopy

Dielectric analysis involves qualitative and quantitative study of induced polarization; developed due to shifting of atoms, ions and thereby + ve/−ve charge centers under an external static or alternating electric field. If the excitation frequency approaches the characteristic or natural frequency of the constituent oscillators, resonance occurs. Whereas relaxation takes on temporizing to overcome the electrical inertia. Frequency-dispersive resonance and relaxation along with impedance spectra introspect the very nature of the constituents with distinct electrical attributes, such as space charge effects, interfacial polarization, inhomogeneous grain core/boundary structures, etc. Complex impedance can be presented as,

$$\hat{Z} = |Z|e^{j\theta} = Z' + jZ'', j = \sqrt{-1}. \tag{5}$$

Here, $|Z|$ is the magnitudes of impedance, θ is the corresponding phase, Z' and Z'' are the gross resistance and

reactance. The real part of complex permittivity (estimates the energy storage capability) can be calculated using the capacitance dispersion as, $\varepsilon' = Cd/\epsilon_0 A$, where C represents the capacitance of the MIM pellet of width d and effective electrode area A, $\epsilon_0 = 8.854 \times 10^{-12} Fm^{-1}$ is the permittivity of free space. The dissipation factor (D) or dielectric loss tangent emphasizes the relaxation loss due to the phase lag

of the oscillating dipoles, in reference to the input waveform, given by the following ratios:

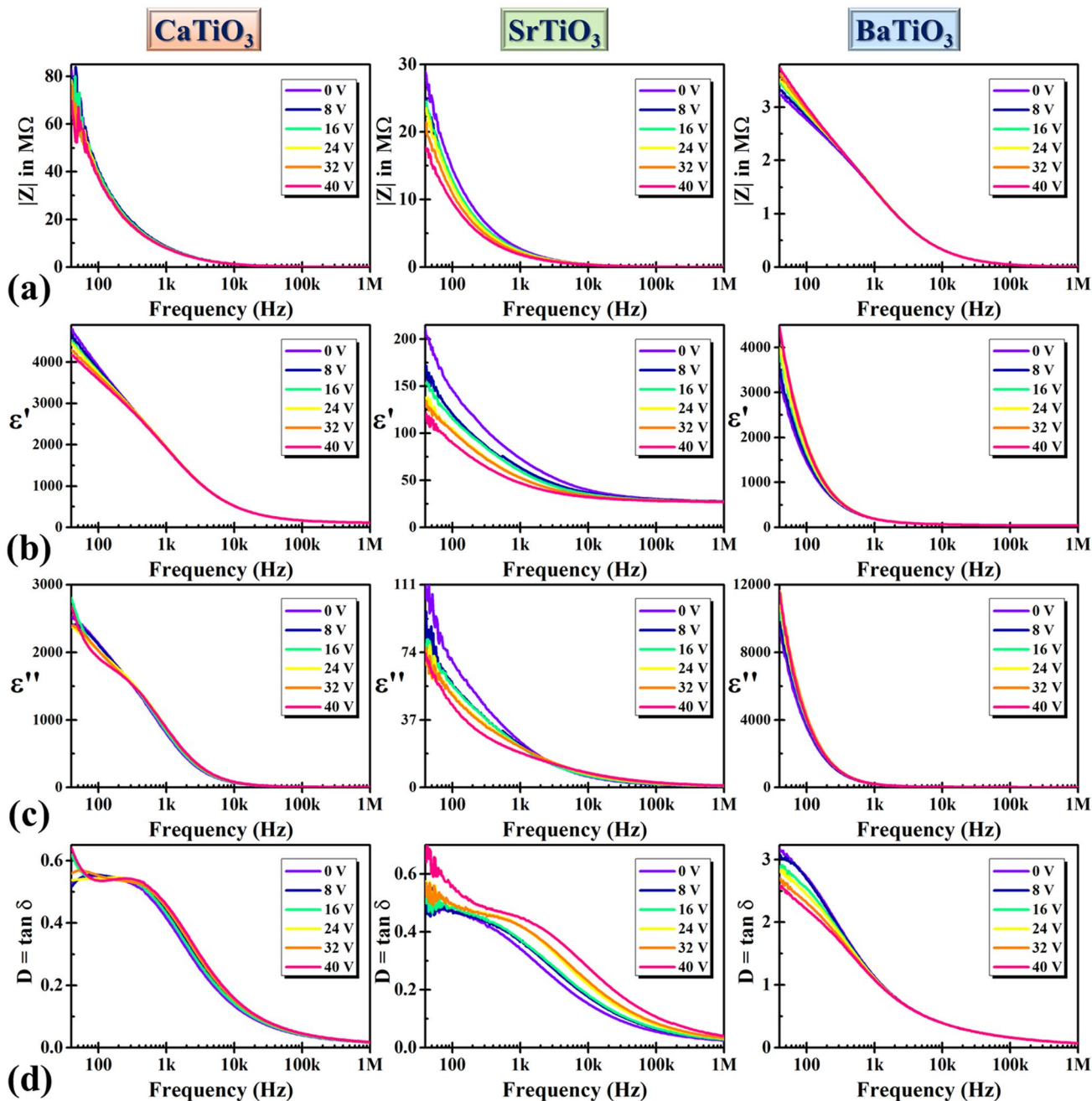$$D = \tan\delta = \frac{Z'}{Z''} = \frac{G}{B} = \frac{\varepsilon''}{\varepsilon'} = \frac{M''}{M'} = \frac{1}{Q_u}. \quad (6)$$

Fig. 5 Bias-dependent frequency dispersions: **a** magnitude of impedance ($|Z|$); **b** real part of dielectric constant (ε'); **c** imaginary part of dielectric constant (ε''); **d** dissipation or loss-factor ($D = \tan\delta$). The three columns respectively demonstrate data for CT, ST and BT. All following figures sustain this mode of presentation

The terms G, B, M' and M'' respectively represent the real and imaginary parts of complex admittance and dielectric modulus (discussed in Sects. 3.7 and 3.8), and Q_u is called the quality factor. The imaginary dielectric constant (a measure of thermal dissipation) is calculated from,

$$\varepsilon'' = \varepsilon' \tan\delta = \frac{Cd}{\epsilon_0 A}\tan\delta. \tag{7}$$

The frequency dispersions of the as-discussed parameters are demonstrated in Fig. 5, S3 and S4 for all three samples under varying applied bias. The rapid and monotonic decay in lower frequencies is consistent with Koop's phenomenological theory [40], which ultimately settles down to a quasi-constant high-frequency limit under dominant electronic and atomic contributions. Below the kHz order frequencies, the induced (dielectrics) or spontaneous (ferroelectrics) dipoles easily follow the input ac sweeps. The in-phase response allows the system to get fully polarized and develops a large dielectric constant or associated parameters. But, synchronizing with the driving signal gets increasingly difficult at higher frequencies (especially for orientational polarization), *i.e.*, the input field gets reversed, before the polarization is built. The resulting delay exhibits nominal polarization and manifests the sharp decay in the dispersions, resembling the very nature of MWIP. Semiconducting grains offer idealistic dielectric features, while properties of insulating grain boundaries are influenced by traps, dislocations and defects. Due to the dominance of grain boundaries at lower frequencies, electrons require greater energy for hopping, that substantiates the high dielectric loss [41].

For all the dispersions, the low-frequency MWIP-dominated regime is immensely field-dependent. However, with frequency dielectric parameters gradually become reluctant to the applied field, because the dipoles vibrate so fast that the applied (moderate) field fails to align them effectively in the appropriate direction. Having a smaller resistivity than CT, ST exhibits significantly greater sensitivity to similar applied bias. The variations of phase angle are typically associated with the state of polarization. In both these samples, drop in $|Z|, Z'$ & R_s under increasing field is obvious. The equivalent series resistance or ESR (R_s) stipulates the net effect of unipolar field on the GC–GB assembly. This nature indicates, the release of space charges in addition to a reduction in barrier height and surge in ac conductivity. Contrarily, BT displays an opposite bias-dependency in reference to CT or ST. This is because of the ferroelectric phase, which although accommodates a lesser compositional fraction, is indeed much more electrically active than the paraelectric counterpart. The external static field builds up polarization in BT, which overshadows other responses and empowers the contribution of bound charges and resistive features. The magnitude of

Z'' typically accompanies relaxation peaks at frequencies that match the hopping frequency of localized electrons. For CT and ST, the trend of data implies that, the peaks are located at very small frequencies (beyond our operating range), while the peak for BT rests near 1 kHz, which undergoes additional broadening for larger bias.

Both the dispersions of ε' and ε'' decrease with bias for CT and ST, *i.e.*, the net energy storage and dissipation fall, which in turn mildly increase the loss tangent. However, BT presents an exact opposite trend, as surface polarization boosts up electric potential energy. For polar dielectrics, the phenomenological Johnson relation is a reasonable approximation for the bias-dependent dielectric constant:

$$\varepsilon'(E) = \frac{\varepsilon'(0)}{\left[1 + \lambda\left\{\epsilon_0\varepsilon'(0)\right\}^3 E^2\right]^{1/3}}. \tag{8}$$

Here λ is a temperature-dependent parameter, and $\lambda\left\{\epsilon_0\varepsilon'(0)\right\}^3 E^2 < 1$ for most practical cases [33, 34]. So, this nonlinear relationship behaves linearly for small to moderate range of fields, see Fig. 6a.

$$\frac{d\varepsilon'(E)}{dE} = -\frac{2}{3}\frac{\lambda\epsilon_0^3\left\{\varepsilon'(0)\right\}^4 E}{\left[1 + \lambda\left\{\epsilon_0\varepsilon'(0)\right\}^3 E^2\right]^{4/3}}. \tag{9}$$

The slope is negative and proportional to the applied electric field in small E limit. ST obviously offers steeper fitted lines than CT. However, if multiple polarization mechanisms superpose or condensation of polar clusters prevails, this empirical model or the simplified LGD theory fails to cumulatively explain the $\varepsilon'(E)$ behavior. The dielectric constant is observed to increase with bias for multifaceted polarization in BT, in accordance with the smaller dissipation factor, that shows the more ordered dipolar conformation. It is especially useful in nanoelectronics, where dielectric tunability is essential against a reduced dissipation.

Molecular dipoles and their relaxation dynamics can be introspected using different models. The oldest is the Debye relaxation theory, which ascertains the dielectric response of an ensemble of ideal and non-interacting dipoles as a function of the excitation (angular) frequency: $\omega = 2\pi f$, f being the linear frequency (in Hz).

$$\hat{\varepsilon}(\omega) = \varepsilon_\infty + \frac{\Delta\epsilon}{1 + j\omega\tau} = \left(\varepsilon_\infty + \frac{\Delta\epsilon}{1 + \omega^2\tau^2}\right) \\ - j\left(\frac{\omega\tau\Delta\epsilon}{1 + \omega^2\tau^2}\right) = \varepsilon' - j\varepsilon'', \tag{10}$$

where $\Delta\epsilon = \varepsilon_s - \varepsilon_\infty$ is the dielectric strength, i.e., the difference of saturated and high-frequency limits and τ is the relaxation time, i.e., the time taken by the oscillating dipoles
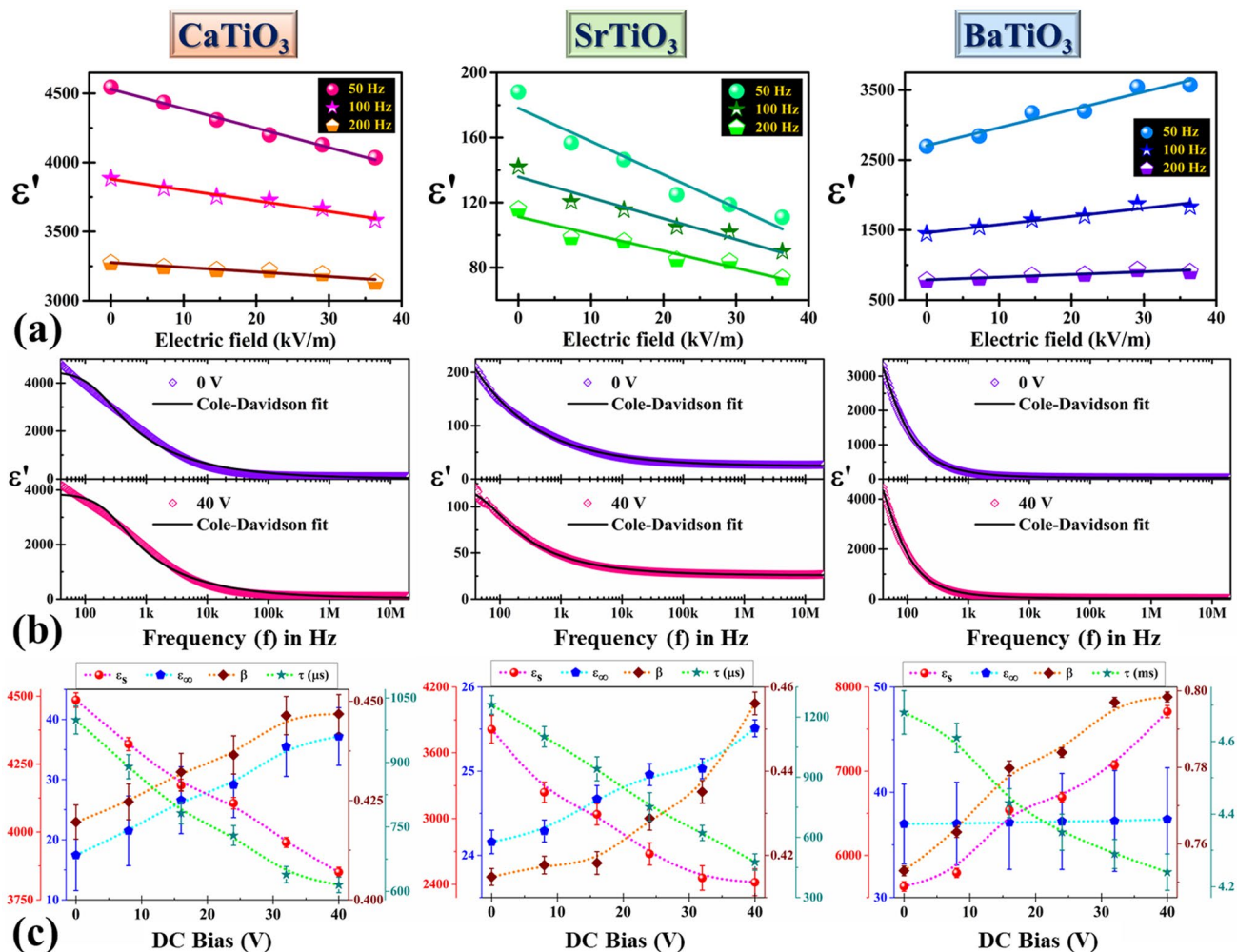
Fig. 6 **a** Linear fits of field-dependent ε' at 50, 100 and 200 Hz input frequency; **b** Cole–Davidson model-based fitting for $\varepsilon'(f)$ dispersion under application of 0 and 40 V bias; **c** bias dependency of the parameters, extracted from best fit: ε_s (red), ε_∞ (blue), β (maroon) and τ (green). The dotted lines are guide to the eye

to align themselves in the direction of the external field or the restoration time to establish equilibrium after the field is withdrawn. However, feasible interactions take place among the adjacent dipoles or with the environment in all practical cases that accompany a distribution of relaxation times and thus asymmetrically broadened loss peaks [42]. A shape parameter: $\beta(0 \leq \beta \leq 1)$ is introduced in the relaxation equations of Cole–Davidson model to account such disparities:

$$\hat{\varepsilon}(\omega) = \varepsilon_\infty + \frac{\varepsilon_s - \varepsilon_\infty}{(1 + j\omega\tau)^\beta}. \tag{11}$$

For $\beta = 1$, Debye's form having a single relaxation time is reobtained. Substituting, $\phi = \tan^{-1}\omega\tau$ and $1 + j\omega\tau = e^{j\phi}\sqrt{1 + \omega^2\tau^2} = e^{j\phi}/\cos\phi$; the simplified ε' turns up as:

$$\varepsilon'(\omega) = \varepsilon_\infty + (\varepsilon_s - \varepsilon_\infty)(\cos\phi)^\beta \cos\beta\phi. \tag{12}$$

The dispersions of the real dielectric constant are thus fitted for different bias using Cole–Davidson model, see Fig. 6b. All the extracted parameters $(\varepsilon_s, \varepsilon_\infty, \beta \& \tau)$ are plotted in Fig. 6c as a function of bias voltage. For all three samples, τ decreases with bias, while β is seen to increase. As the steady field increases, the electric potential energy of the conjugated charge ensemble also increases. Therefore, all relaxation mechanisms speed up resulting a monotonic increase in τ. Moreover, the steady unipolar field orients the dipoles more uniformly, which enables them to relax archetypically. So, the Debye model attains more relevance and the proper fraction β approaches unity. Now for CT and ST, ε_s decreases as prescribed by the Johnson relation, while a small but steady enhancement in ε_∞ is found. This indicates, at higher frequencies, a positive correlation persists between
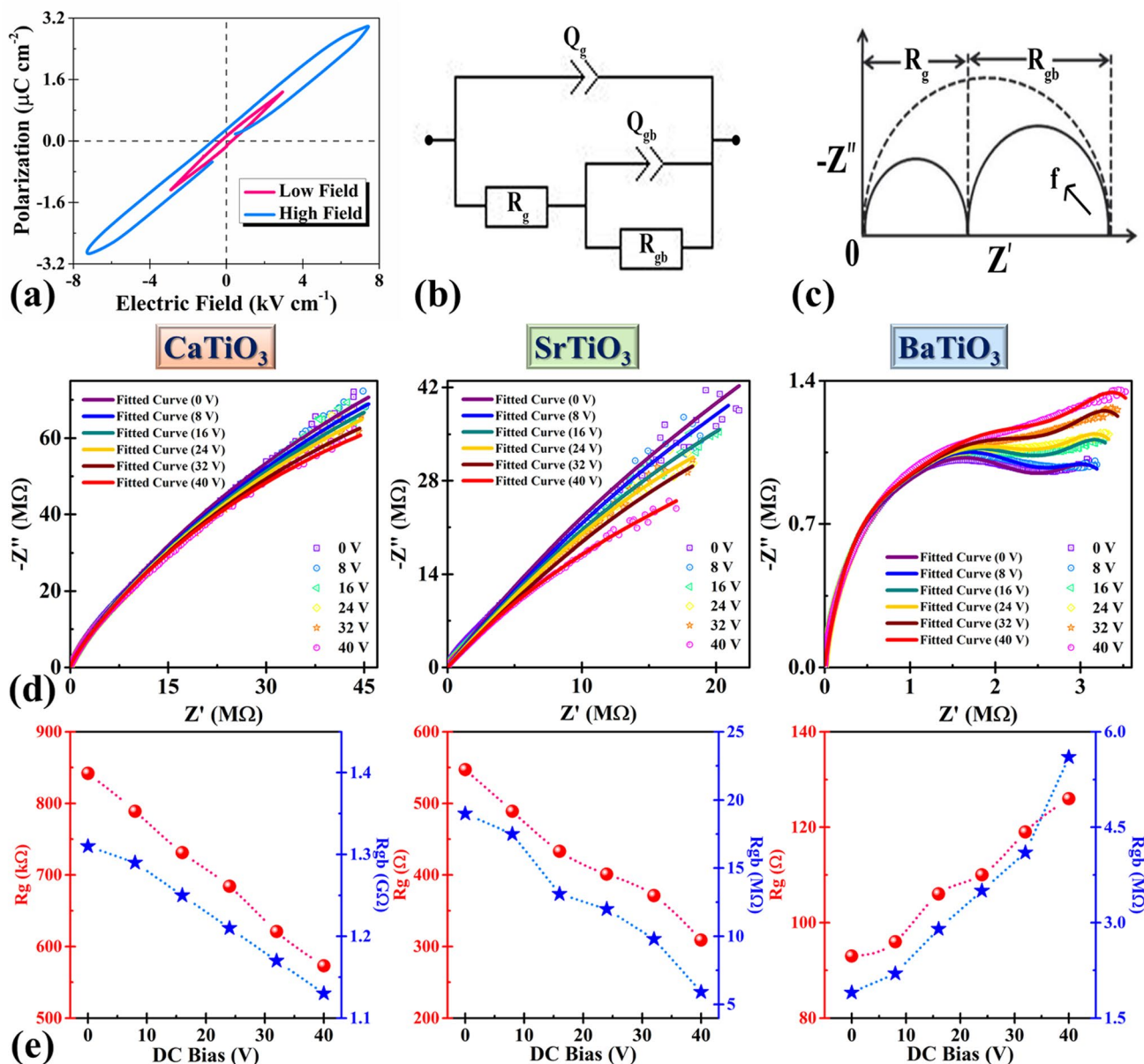
Fig. 7 a $P-E$ hysteresis loops for BT under a low and a high field cycle; **b** schematic of the as-deployed equivalent circuit model, comprising two pairs of resistors and constant phase-elements; **c** theoretical prediction of Nyquist plots from this model; **d** experimentally obtained Nyquist plots under distinct field conditions; **e** variation of R_g and R_{gb} (extracted from the fitted curves) as a function of external bias. The dotted lines are guide to the eye

permittivity and external field. However, for BT, such correlation is very weak and ε_∞ remains almost bias-independent. Contrarily, ε_s monotonically increases with bias voltage for the induced polarization in agreement with the results of Fig. 6a. Ferroelectric nature of the tetragonal phase of BT is further verified from the $P-E$ hysteresis loops at two different field strengths, as shown in Fig. 7a. The loops do not resemble ideal ferroelectric features, because the sample contains a preponderant paraelectric phase with no hysteretic property [43]. The respective remanent polarizations for the two strengths are 0.17 and 0.32 $\mu C\ cm^{-2}$.

The transport properties, resistivity correlations and grain core/boundary structure can be retrospectively probed by analyzing Nyquist plots. Such a core-boundary constitution can be modeled with an equivalent circuit [30, 35]; employing two pairs of resistors (R) and constant phase elements (Q)

as shown in Fig. 7b. As two distinct electrical entities viz., grains and grain boundaries contribute to the dielectric properties, and the grains have significantly smaller resistivity offering greater contribution in the transport than the grain boundaries, the attributes of the grains and grain boundaries are represented by $(R_g, Q_g) \& (R_{gb}, Q_{gb})$. Furthermore, as grains are embedded in the grain boundary matrix, one $R - Q$ sub-network is inscribed within the other to construct such an interlinked circuit model that renders the system physically. The capacitance (C) corresponding to an element (R, Q) can be computed given the distributing factor (α) that stands for the deviation from a pure capacitor as a result of non-Debye relaxations and asymmetric broadening.

$$C = R^{\frac{1-\alpha}{\alpha}} Q^{\frac{1}{\alpha}}. \tag{13}$$

Generally, space charge effects or MWIP occurs when mobile carriers get impeded by a physical barrier, *i.e.*, the grain boundary, which notably inhibits charge migration [18, 44]. Subsequently, charges pile up to produce a localized polarization at the GC–GB interface. The expression for complex impedance in this formalism takes the from:

$$\hat{Z}(\omega) = \frac{R_{gb} + R_g \left\{ 1 + (j\omega)^{\alpha_{gb}} Q_{gb} R_{gb} \right\}}{1 + (j\omega)^{\alpha_{gb}} Q_{gb} R_{gb} + (j\omega)^{\alpha_g} Q_g \left[R_{gb} + R_g \left\{ 1 + (j\omega)^{\alpha_{gb}} Q_{gb} R_{gb} \right\} \right]}. \tag{14}$$

This model circuit simulates a Nyquist curve comprising two semi-circular arcs like Fig. 7c, that outlines each pair of $R - Q$ subsystems enduring Debye relaxations. But if the electrically active regions are not well-resolved or offer close credentials, the couple of semi-circles superposes and develops a single distorted semi-ellipse, which assents the Cole–Davidson model [45].

The Nyquist plots are thus fitted against this circuit model for various applied fields employing the EC-Lab software, ensuring satisfactory least-squares goodness-of-fit (< 0.1), see Fig. 7d. For BT, two distinct semi-circles can be recognized. The non-requirement of external elements to fit the experimental data reflects absence of any appreciable electrode polarization effect. The low-frequency regime is field-sensitive and manifests MWIP involving domain wall motion [30]. However, the high-frequency bias-independent region can be ascribed to phonon-assisted electron hopping at the adiabatic limit. The extracted resistances $R_g \& R_{gb}$ are plotted as a function of bias voltage in Fig. 7e. Typically, ceramic oxides accommodate point defects, e.g., vacancies and traps. As the applied field increases, the charge carriers trapped in such potential wells acquire electrostatic energy and eventually extricate. Subsequently, ESR drops against a smaller bound-to-free carrier ratio. For the pure dielectric CT/ST phases, the grain core and boundary resistances thus decrease with bias. However, BT having a ferroelectric phase delivers a counter effect, where the polarization

pursuit led by bound charges predominates. Hence, the system gets more resistive with increase in bias that agrees with the dispersions of $|Z| \& R_s$.
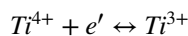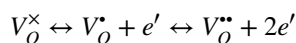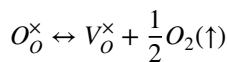
3.7 Admittance spectroscopy

Achieving ideal Ohmic contacts between metal–semiconductor junction is very difficult, due to formation of insulating layers, interfacial roughness or gaps, oxidation, etc. Hence, extracted parameters from impedance and dielectric spectra are never completely devoid of error, as the unmasked low-frequency declining slope is focused. Admittance spectroscopy is a convenient tool to explore high-frequency conduction mechanisms, free from electrode polarization effects. Complex admittance can be mathematically conveyed as:

$$\hat{Y} = \frac{1}{\hat{Z}} = |Y| e^{j\varphi} = G + jB = G + j\omega C, \tag{15}$$

where $|Y|, \varphi, G \& B$ represent the magnitude of admittance, associated phase, real (conductance) and imaginary (susceptance) parts, respectively. In Fig. 8a, b and S3d, parameters dominate in higher frequencies as described in Rezlescue model [46]. At lower frequencies, conductance remains insignificant and almost constant, but as the characteristic 'hopping frequency' is approached, dispersion takes place.

Application of bias has very mildly increased $|Y| \& G$, and lowered B nominally for the first two samples. The field-assisted growth in carrier density is likely responsible for this. For BT, however, the trend is exactly opposite for the aforementioned reasons. Here the dispersions do not get influenced by the deep traps, as the corresponding release rates $(\ll 1 s^{-1})$ are rejected in the operational frequency regime. Under applied field, $3d$ electrons can hop from Ti^{3+} to Ti^{4+} ions in the family of titanates and vice versa. This multiple valency of transition metal ions is often coupled with oxygen vacancies [18, 47]. Using Kröger–Vink notation, their dynamics can be summarized as:

$$O_O^\times \leftrightarrow V_O^\times + \frac{1}{2} O_2 (\uparrow)$$

$$V_O^\times \leftrightarrow V_O^\bullet + e' \leftrightarrow V_O^{\bullet\bullet} + 2e'$$

$$Ti^{4+} + e' \leftrightarrow Ti^{3+}$$

Hence, the arrangement of ions in the crystal largely controls the electron hopping mechanism and the mobility of carriers. Such mechanisms generally operate over a certain cryogenic temperature, below which all vacancy defects are 'frozen-in' [18]. At room temperature, a
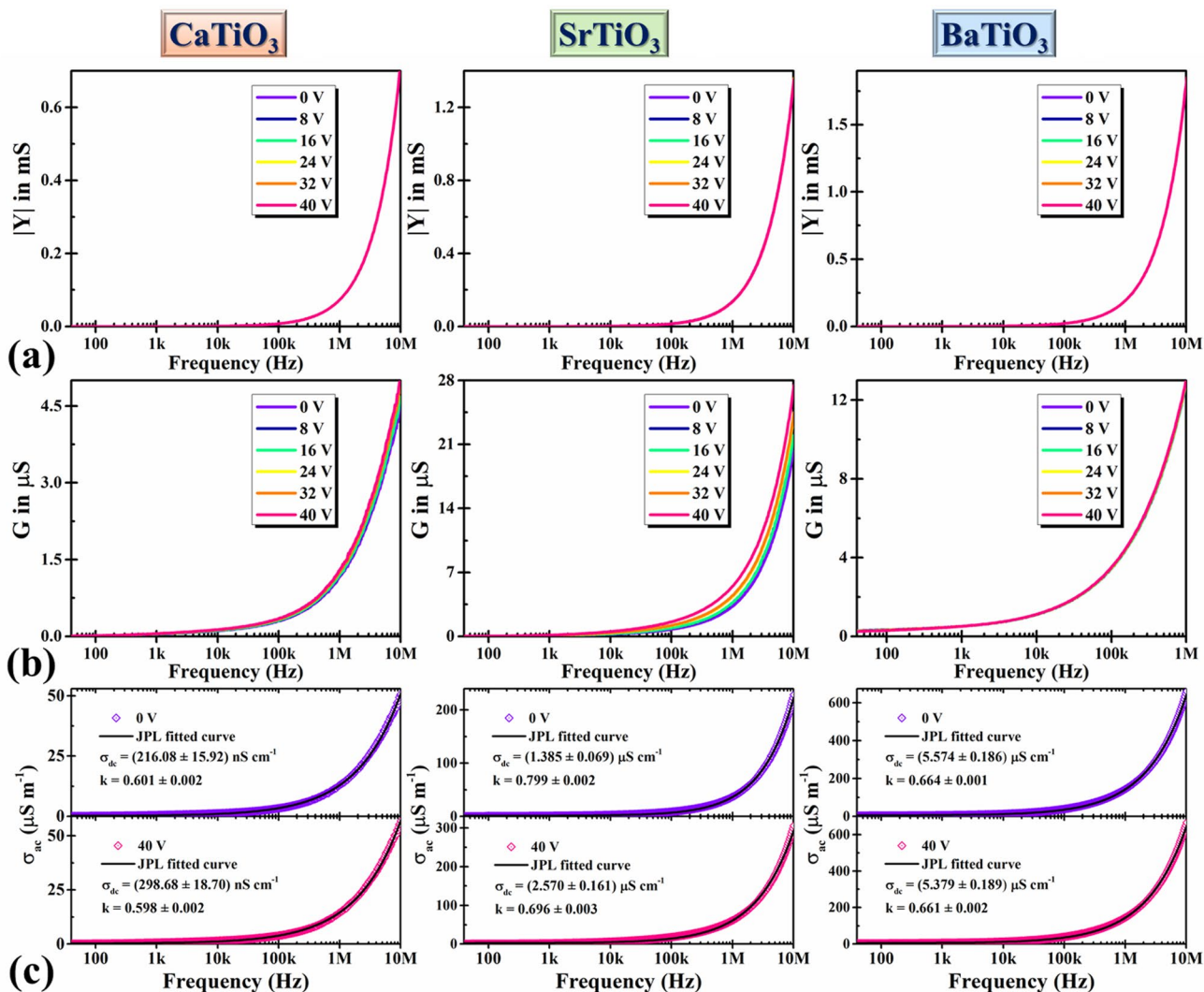
Fig. 8 Bias-dependent frequency dispersions: **a** magnitude of admittance ($|Y|$); **b** conductance (G); **c** Jonscher's power law (JPL) fitting of ac conductivity (σ_{ac}) at nil and 40 V applied bias

significant fraction of the trapped carriers gets thermally activated and takes part in hopping and diffusion [48]. They even condense to form polar clusters, as it is energetically favorable to aggregate into clusters to reduce distortion energy.

Now, the nature of mobile carriers can be further examined by studying ac conductivity:

$$\sigma_{ac} = \varepsilon_0 \varepsilon'' \omega = \varepsilon_0 (\varepsilon' \tan\delta) \omega = \frac{Gd}{A}. \tag{16}$$

Frequency dependence of σ_{ac} can be described by the well-known Jonscher's power law (JPL) [49]:

$$\sigma_{ac}(f) = \sigma_{dc} + \sigma_0 f^n, \tag{17}$$

where σ_{dc} stands for the extrapolated dc conductivity, σ_0 is a weighting constant related to the polarizability strength and n is the frequency exponent. The first term indicates excitation of some electrons to the conduction band from a localized state and their drift mobility, while the second one represents dielectric relaxation of bound or localized charges. All these parameters depend not only on the material, but also on external field and temperature [30, 41]. The exponent entails the degree of interaction between charge carriers and the surrounding lattice. Identification of different conduction mechanisms in semiconductors, *e.g.*, correlated-barrier and variable-range hopping, overlapped polaron tunneling, quantum tunneling, etc. is based on the field and temperature dependency of n. Figure 8c displays fitting of conductivity dispersions (0 and 40 V) using JPL, and the extracted parameters are enumerated in Table 5. For

Table 5 Extracted parameters from JPL fitting of frequency-dispersive conductivity

DC Bias (V)	CT		ST		BT	
	σ_{dc}(nS cm^{-1})	n	σ_{dc}(µS cm^{-1})	n	σ_{dc}(µS cm^{-1})	n
0	216.08 ± 15.92	0.601 ± 0.002	1.385 ± 0.069	0.799 ± 0.002	5.574 ± 0.186	0.664 ± 0.001
8	236.58 ± 13.11	0.601 ± 0.001	1.461 ± 0.085	0.781 ± 0.002	5.560 ± 0.153	0.664 ± 0.002
16	243.98 ± 16.00	0.600 ± 0.001	1.651 ± 0.182	0.759 ± 0.003	5.513 ± 0.154	0.664 ± 0.002
24	261.23 ± 10.16	0.599 ± 0.002	1.893 ± 0.099	0.747 ± 0.003	5.468 ± 0.205	0.663 ± 0.001
32	284.51 ± 14.12	0.598 ± 0.002	2.111 ± 0.121	0.713 ± 0.003	5.412 ± 0.201	0.662 ± 0.002
40	298.68 ± 18.70	0.598 ± 0.002	2.570 ± 0.161	0.696 ± 0.003	5.379 ± 0.189	0.661 ± 0.002

CT and ST, dc conductivity rises with external field, while BT shows an opposite trend due to the enlarged polarization and insubstantial delocalization of carriers. However, for all three materials, the exponent has decreased monotonically with bias. Such values of $n (\leq 1)$ are indicative of concurrent translational and hopping dynamics of charge carriers, according to Funke [50, 51]. In his jump relaxation model (JRM), it was proposed that, the ions can make successful hops to vacant neighboring sites for low frequency due to availability of sufficient time intervals. This gives rise to a long-range translational motion of ions, devoted to σ_{dc}. Contrarily, both successful and unsuccessful hopping take place in the high-frequency regime. The jumping ions can either jump back to the initial site, or may jump to a new position for a stable relaxation. The former is considered unsuccessful, while the latter is designated as a successful hop. In the high-frequency end, the ratio of successful and failed hops increases, leading to a dispersive conductivity.

For CT and ST, the respective correlated-barrier hopping (CBH) and variable-range hopping (VRH) model more precisely explain the exact features of conduction mechanism [18, 52, 53]. Here, large polaron hopping is considered responsible for the conduction, where two polarons hop over the potential barrier simultaneously between charged trap/defect states and $n(T)$ varies as:

$$n = 1 - \frac{6k_B T}{W_m + k_B T \ln\left(\omega \tau_0\right)}, \tag{18}$$

where W_m is the binding energy of the carrier and k_B is the Boltzmann constant. The synergism of hopping electrons and ionized oxygen vacancies generates polaronic relaxations and evinces as-obtained field-dependency of σ_{dc} & n. Large polarons can polarize more neighboring sites than small polarons and propagate with greater effective mass. The increase in n with bias supports that. In this model, Coulombic interactions correlate the barrier height with the inter-site separation.

3.8 Modulus spectroscopy

Finally, the complex electric modulus $\left(\hat{M}\right)$ is studied to analyze the unwinding of the electric field through the space charge distribution against a fixed dielectric displacement. Macedo proposed this technique to suppress all low-frequency electrode effects completely and compute relaxation parameters of the medium seamlessly [41, 54]. Considering the dielectric constant as an electrical analog of mechanical shear modulus, $\hat{M}$ is defined by,

$$\begin{aligned}
\hat{M} &= \frac{1}{\hat{\varepsilon}} = \frac{1}{\varepsilon_\infty}\left[1 - \int_0^\infty e^{-j\omega t}\left\{\frac{d\psi(t)}{dt}\right\}dt\right] \\
&= \left(\frac{\varepsilon'}{\varepsilon'^2 + \varepsilon''^2}\right) - j\left(\frac{\varepsilon''}{\varepsilon'^2 + \varepsilon''^2}\right) \\
&= M' - jM'',
\end{aligned} \tag{19}$$

where the function $\psi(t) = \psi(0)e^{-(t/\tau_0)^\eta}$ outlines time evolution of the electric field inside dielectrics. The stretched exponent η is a proper fraction and τ_0 is the associated relaxation time. The frequency-dispersive real $\left(M'\right)$ and imaginary $\left(M''\right)$ parts are shown in Fig. 9 for different bias fields. M' has some inclusive features: (a) it has a nominal value in the low-frequency regime, (b) as the frequency elevates, the dispersion approaches an asymptotic maximum: $M_\infty = 1/\varepsilon_\infty$, (c) the sigmoidal nature is related to the carrier-mobility over a long range against the as-neglected electrode polarization, (d) the effect of applied field is hard to detect, instead for ST, where a small, but steady hike in M' is found.

$M''(f)$ on the other hand, exhibits a distinct and broad peak across few kHz to few tens of kHz order with perceptible bias dependency. This is the frequency regime, where carrier hopping in between neighboring sites and/or carrier-motion restricted within the short range of potential wells contend over longer distances. For all three samples, the bands rise and shift toward higher frequencies with increase in applied field, although the effect is nominal for BT. As mentioned earlier, non-Debye relaxation causes asymmetric broadening of the bands, that can be further scrutinized
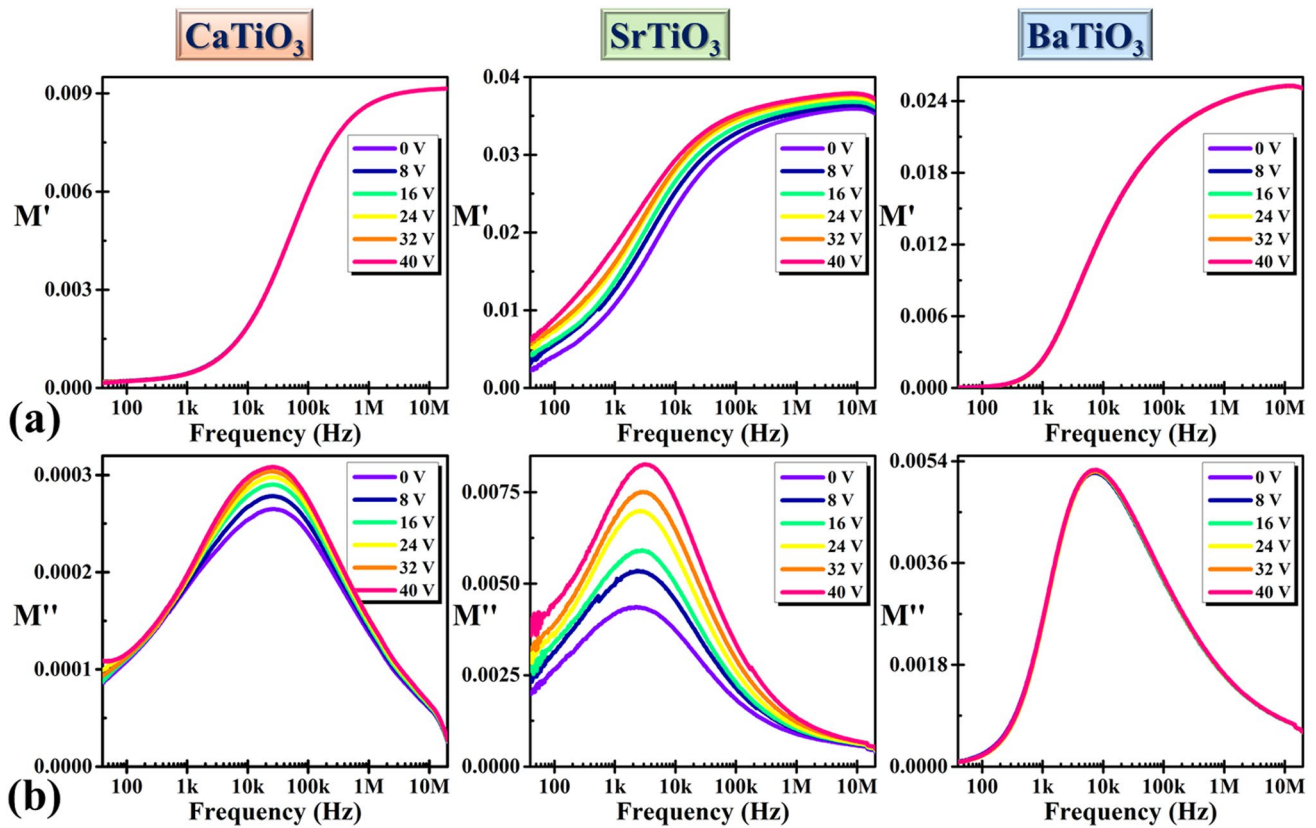
Fig. 9 Bias dependence of **a** real and **b** imaginary part of frequency-dispersive dielectric modulus $\left(\hat{M}\right)$

using the modified Kohlrausch–Williams–Watts (KWW) function:

$$M''(f) = \frac{M''_{max}}{\left(\frac{1-c}{a+b}\right)\left\{b\left(\frac{f_{max}}{f}\right)^a + a\left(\frac{f}{f_{max}}\right)^b\right\} + c}. \quad (20)$$

Here two independent shape-parameters: a&b are used to describe the low and high-frequency regime, along with a smoothing parameter (c) regarding a generalized susceptibility function, as proposed by Bergman [55]. All $M''(f)$ dispersions are thus fitted using this model to compute a, b, c, f_{max} and M''_{max}. Fitted curves for the two extreme fields are shown in Fig. 10a. a, b and M''_{max} are enunciated in Table 6 for all samples, while the computed values of $c \approx 0 \left(< 10^{-10}\right)$. For calcium and strontium compounds, a&b are seen to increase with bias, which typically assists the ideal Debye-type properties. However, a tiny, but complex change was recorded for BT. Here a (characterizes higher frequencies) deviates more from unity, while b (represents small frequencies) nominally increases with bias. This is because, with applied field, the dipoles reorient to mimic a more orderly structure. However, the nonlinear (ferroelectric) characteristics get boosted. The characteristic relaxation

time can be computed using $\tau_0 = 1/f_{max}$. Figure 10b demonstrates how f_{max} blue shifts against bias, which eventually leads to a monotonic decrement in τ_0. It is important to emphasize that, this τ_0 is different from the τ elaborated in Sect. 3.4 and Fig. 6. The combination of dielectric, admittance and modulus spectroscopy is exceptionally powerful, because they characterize relaxation or conduction properties of distinct frequency regimes. While the first two respectively explain properties at the low- and high-frequency end, modulus spectra furnish information for the regime in between. The carrier dynamics and relaxation mechanisms too are distinct at different frequencies. Naturally τ_0&τ belong to different order, although speculate similar trends against bias.

Finally, the normalized dispersion of the imaginary part $\left[\frac{M''(f)}{M''_{max}}\right]$ is plotted versus normalized frequency $\left(\frac{f}{f_{max}}\right)$ for the samples under all fields in Fig. 10c. The fact that, all curves nearly overlap on each other in the reduced form and can be scaled to a master curve, suggests that the fundamental dynamics of relaxation mechanism is identical under all fields [41, 53]. Taking $a = b = 1$ and $c = 0$, the universal Debye response (UDR) is retrieved:
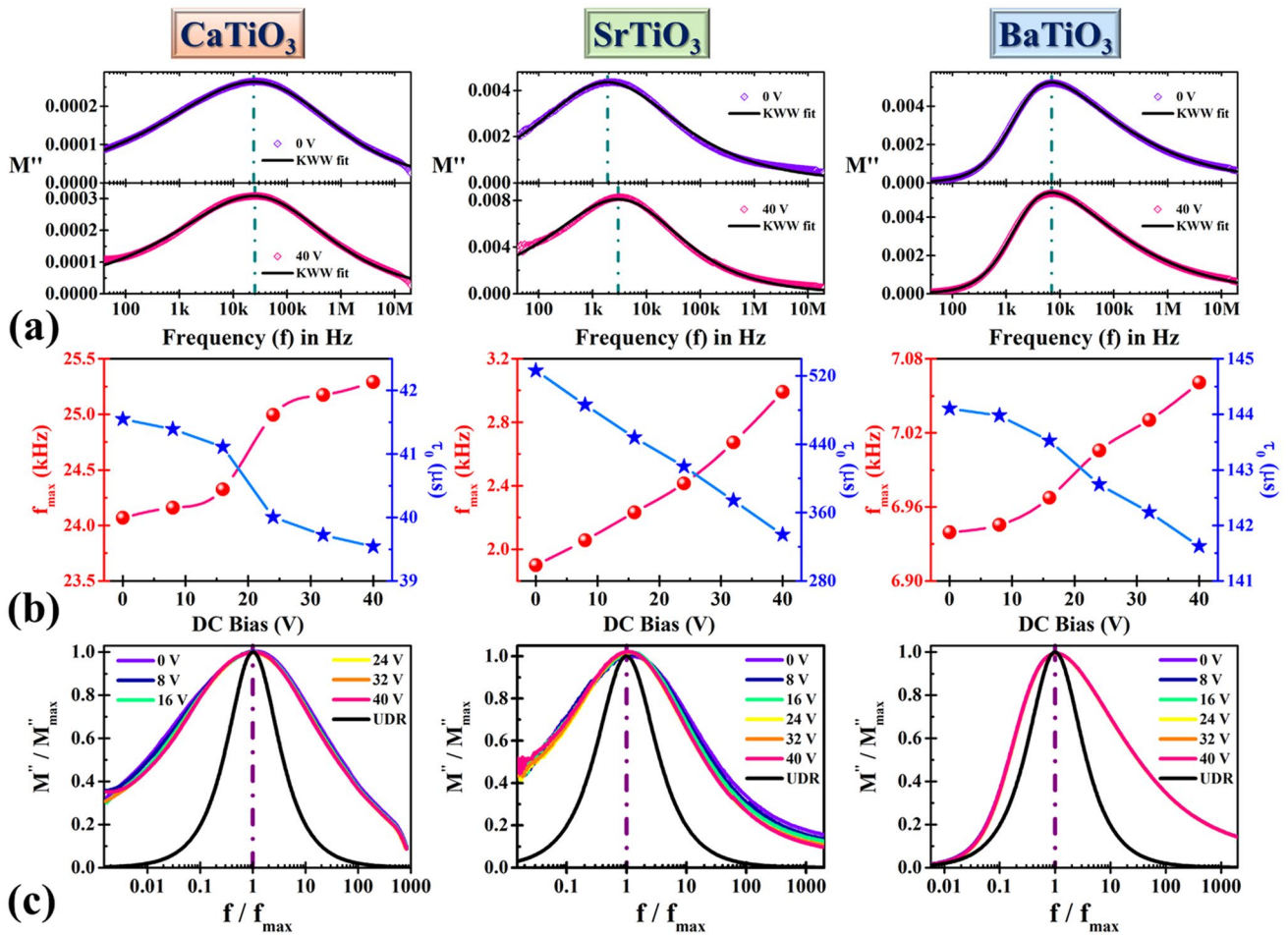
Fig. 10 **a** Modified KWW fits for $M''(f)$ dispersion at nil and 40 V bias; **b** bias dependency of as-obtained f_{max} and τ_0; **c** normalized imaginary electric modulus M''/M''_{max} versus f/f_{max} under varying fields in reference to the ideal Debye response (black curve)

Table 6 Extracted shape parameters (a&b) and M''_{max} from modified KWW fitting of the imaginary part of frequency-dispersive electric modulus

DC bias (V)	CT			ST			BT		
	a	b	$M''_{max} \times 10^4$	a	b	M''_{max}	a	b	M''_{max}
0	0.2184(4)	0.4079(0)	2.63(9)	0.3794(5)	0.3560(9)	0.0043(5)	1.2354(7)	0.3841(0)	0.0052(2)
8	0.2419(3)	0.4093(1)	2.77(9)	0.3930(0)	0.3868(6)	0.0052(9)	1.2487(8)	0.3842(6)	0.0052(4)
16	0.2520(3)	0.4183(3)	2.90(0)	0.4173(5)	0.4136(9)	0.0058(0)	1.2566(1)	0.3854(0)	0.0052(5)
24	0.2760(8)	0.4157(3)	2.97(1)	0.4320(3)	0.4376(2)	0.0068(5)	1.2600(6)	0.3864(1)	0.0052(7)
32	0.2840(6)	0.4181(0)	3.04(3)	0.4367(6)	0.4443(6)	0.0073(7)	1.2675(9)	0.3882(4)	0.0052(8)
40	0.3043(0)	0.4279(0)	3.08(5)	0.4471(9)	0.4695(3)	0.0080(9)	1.2746(0)	0.3884(4)	0.0052(9)

$$M''(f) = \frac{M''_{max}}{\frac{1}{2}\left(\frac{f_{max}}{f} + \frac{f}{f_{max}}\right)}. \tag{21}$$

In reference to UDR (FWHM = 1.144 dB), the asymmetric broadening can be clearly recognized. This FWHM has an inverse relationship with the coefficient η, i.e., the more the broadening, the more is the deviation of η from unity.

For CT and ST, the broadening is dominated in the lower frequencies, i.e., the left width is higher than the right width in the peaks. But BT opts an opposite picture, where the curve has widened more at the high-frequency side (results $a > 1$). This is speculated by the diffusive nature of the
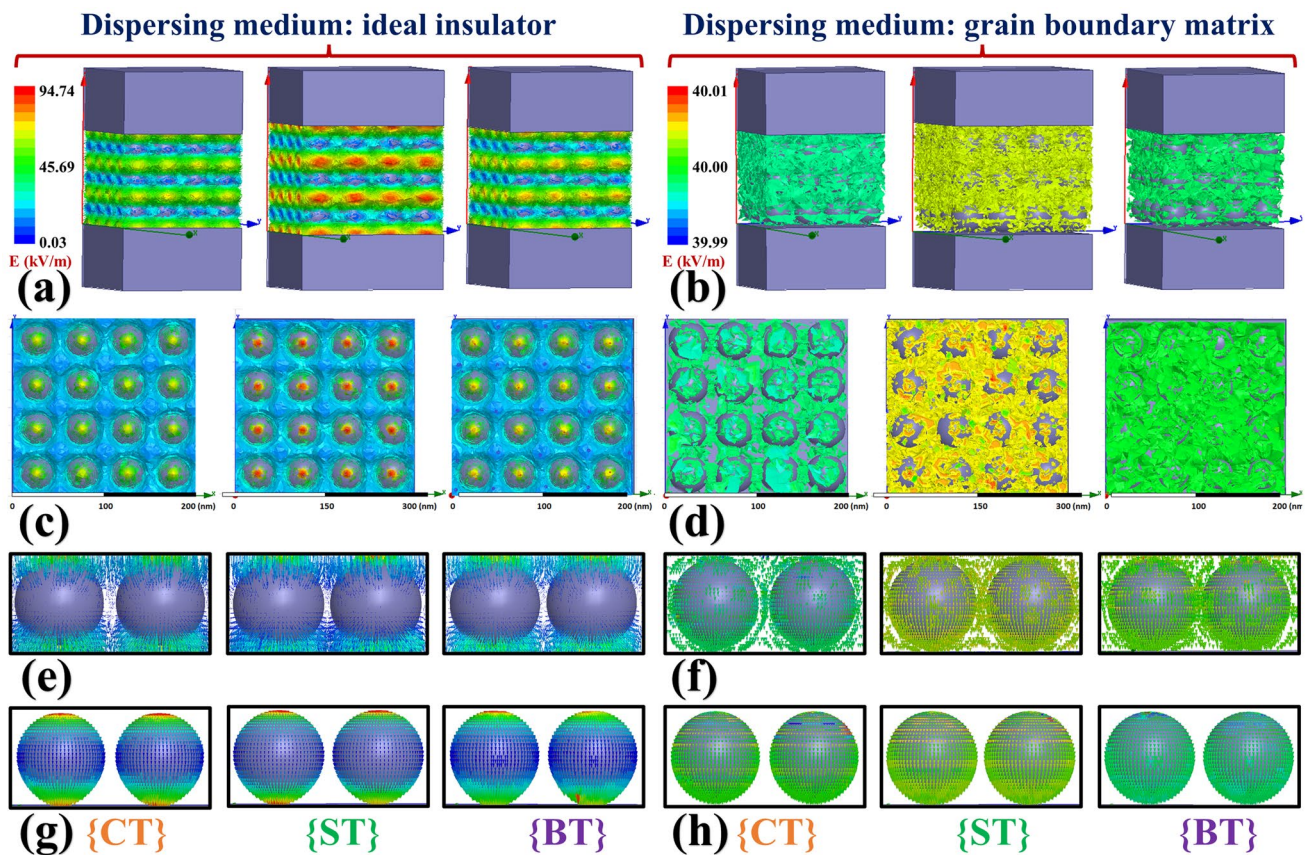
Fig. 11 Electric field map in the GC–GB architecture depicted for the ideal insulator (left panel) and grain boundary material (right panel), serving as the dispersing medium for the three respective compounds.

Magnitude of applied field: **a**, **b** side view and **c**, **d** top view. Magnified view for distribution of **e**, **f** electric field vectors outside the grains and **g**, **h** displacement vectors within the grains

associated oscillators, that adversely respond to respective lower or higher energy excitations.

3.9 Electric field distribution from finite element simulation

The simulations are carried out based on a few rudimentary assumptions and propositions: (a) semiconducting grains are embedded in insulating grain boundary host and the GC–GB interface is sharply defined, (b) the distribution of grains in the dispersing medium is homogeneous and isotropic, (c) the nano-cores are chosen to be spherical owing to the near-spherical morphology of our samples, (d) considering the fact that, crystallites in a polycrystalline nanoparticle polarize distinctly, the nano-core dimensions are set as per the D_{cryst} values obtained from Eq. (1), and (e) a positive voltage is applied at the top electrode keeping the bottom electrode grounded to simulate field conditions similar to the experimental setup, where a maximum of 40 V was applied across the sample pellets.

In theory, grain boundaries are delineated as ideal insulators. However, in practice, they are somewhat congruent

dielectric materials with much smaller conductivity due to defects and gaps. For each case, distribution of field intensity and field/displacement vectors is illustrated in Fig. 11. Some notable observations are: (i) in case of perfect insulator, large field gradient is present in the vicinity of the GC–GB interface, while for the experimentally obtained grain boundary host, a more uniform field distribution can be found, (ii) the variation of electric flux is more pronounced for ST, which gradually reduces for BT and CT. This result is consistent with the experimentally realized sensitivity (ST > BT > CT) of different electrical parameters on dc bias, (iii) because of the finite conductivity of the grain boundary material, the penetration depth of the external field reduces that encompasses a more realistic endeavor, (iv) for feasible GC–GB framework, the net polarization comprehends both components and interfacial polarization develops, (v) owing to the high polarization of the grains, the field lines get weakly attracted toward them and get bent (anisotropy), (vi) the field vectors are more localized to the extreme ends (inhomogeneity) for the perfectly insulating hosts, (vii) the distribution of displacement vectors inside the grains contain their degree of polarization. So, even a homogeneous and isotropic grain

distribution induces a non-uniform, anisotropic deviation at the microscopic level [30].

4 Conclusive remarks

Summarily, crystal structures of the as-synthesized nanoparticles were verified to be orthorhombic for CT, cubic for ST and a 68 ∶ 32 mixture of cubic and tetragonal phases for BT from Rietveld analysis. The field-dependent dielectric and impedance spectra were (a) fitted with Cole–Davidson model to understand the relaxation dynamics and calculate relaxation times, (b) explained in light of phenomenological Johnson relation, and (c) matched with an equivalent circuit model that simulates Nyquist plots analogous to experimental data. The field-dependency of grain/grain boundary resistance and associated IBLC were interpreted in accordance to MWIP and space charge effects. Unlike CT/ST, the dielectric and ferroelectric phases in BT were seen to contest with each other, where the latter governed the outcomes and as-anticipated dielectric features were mostly suppressed. From admittance spectroscopy, the field-induced de-trapping of carriers and polaron hopping conduction were revealed. JPL fits of conductivity dispersions as a function of bias voltage supported quantitative applicability of the CBH and VRH model. Finally, modulus spectra were used to characterize the non-Debye dipolar relaxations, where the subsequent variation of characteristic times, shape parameters and asymmetric KWW broadening of $M''(f)$ peaks with bias were delineated. Theoretical results not only frame experimental background, but also establish microscopic inhomogeneity and electrical anisotropy in the GC–GB environs. A complete set of field-dependent dispersion analysis against a broad radio/audio range for this family of compounds, thus offer a route-map to commendably customize diverse electrical properties in hybrid ceramics to achieve 'bane to boon' device performance.

Supplementary Information The online version contains supplementary material available at https://doi.org/10.1007/s00339-022-05638-2.

Declarations

References

1. K.A. Müller, H. Burkard, Phys. Rev. B Condens. Mater. **19**(7), 3593 (1979)
2. L. Zhang, W. Zhong, Y. Wang, P. Zhang, Solid State Commun. **104**(5), 263–266 (1997)
3. R. Zheng, J. Wang, X. Tang et al., J. Appl. Phys. **98**(8), 084108 (2005)
4. M. Vračar, A. Kuzmin, R. Merkle et al., Phys. Rev. B Condens. Mater. **76**(17), 174107 (2007)
5. P. Victor, R. Ranjith, S. Krupanidhi, J. Appl. Phys. **94**(12), 7702–7709 (2003)
6. S. Qin, X. Wu, F. Seifert, A.I. Becerro, J. Chem. Soc. Dalton Trans. **19**, 3751–3755 (2002)
7. T. Mitsui, W.B. Westphal, Phys. Rev. **124**(5), 1354 (1961)
8. L. Zhang, X. Wang, W. Yang, H. Liu, X. Yao, J. Appl. Phys. **104**(1), 014104 (2008)
9. B. Jiang, J. Iocozzia, L. Zhao et al., Chem. Soc. Rev. **48**(4), 1194–1228 (2019)
10. F. Kang, L. Zhang, B. Huang et al., J. Eur. Ceram. Soc. **40**(4), 1198–1204 (2020)
11. J.T. Last, Phys. Rev. **105**(6), 1740 (1957)
12. Y. Li, X. Gao, G. Li, G. Pan, T. Yan, H. Zhu, J. Phys. Chem. C **113**(11), 4386–4394 (2009)
13. O. Jongprateep, N. Sato, R. Techapiesancharoenkij, K. Surawathanawises, Adv. Mater. Sci. Eng. **2019**, 1–7 (2019)
14. S.S. Arbuj, R.R. Hawaldar, S. Varma, S.B. Waghmode, B.N. Wani, Sci. Adv. Mater. **4**(5–6), 568–572 (2012)
15. A.E. Souza, S.R. Teixeira, C. Morilla-Santos, W.H. Schreiner, P.N. Lisboa Filho, E. Longo, J. Mater. Chem. C **2**(34), 7056–7070 (2014)
16. Y.-I. Kim, J.K. Jung, K.-S. Ryu, Mater. Res. Bull. **39**(7–8), 1045–1053 (2004)
17. A. Maurice, R. Buchanan, Ferroelectrics **74**(1), 61–75 (1987)
18. C. Wang, C. Lei, G. Wang et al., J. Appl. Phys. **113**(9), 094103 (2013)
19. H. Trabelsi, M. Bejar, E. Dhahri et al., Appl. Surf. Sci. **426**, 386–390 (2017)
20. S. Saha, T. Sinha, A. Mookerjee, J. Phys. Condens. Matter **12**(14), 3325 (2000)
21. B. Luo, X. Wang, E. Tian, G. Li, L. Li, J. Mater. Chem. C **3**(33), 8625–8633 (2015)
22. N. Sai, B. Meyer, D. Vanderbilt, Phys. Rev. Lett. **84**(24), 5636 (2000)
23. M. Liu, J. Liu, C. Ma et al., CrystEngComm **15**(34), 6641–6644 (2013)
24. S. Shah, P. Bristowe, A. Kolpak, A. Rappe, J. Mater. Sci. **43**(11), 3750–3760 (2008)
25. P. Thongbai, S. Tangwancharoen, T. Yamwong, S. Maensiri, J. Phys. Condens. Matter **20**(39), 395227 (2008)
26. I. Raevski, S. Prosandeev, A. Bogatin, M. Malitskaya, L. Jastrabik, J. Appl. Phys. **93**(7), 4130–4136 (2003)

27. N. Giri, A. Mondal, S. Sarkar, R. Ray, J. Mater. Sci. Mater. Electron. **31**(15), 12628–12637 (2020)

28. D. Mitra, S. Bhattacharjee, N. Mazumder, B.K. Das, P. Chattopadhyay, K.K. Chattopadhyay, Ceram. Int. **46**(12), 20437–20447 (2020)

29. J.K. Lee, K.S. Hong, J.W. Jang, J. Am. Ceram. Soc. **84**(9), 2001–2006 (2001)

30. S. Bhattacharjee, A. Banerjee, K.K. Chattopadhyay, J. Phys. D: Appl. Phys. **54**(29), 295301 (2021)

31. H. Borkar, V. Rao, M. Tomar, V. Gupta, A. Kumar, J. Alloys Compd. **737**, 821–828 (2018)

32. N. Besra, K. Sardar, N. Mazumder, S. Bhattacharjee, A. Das, B. Das, S. Sarkar, K.K. Chattopadhyay, J. Phys. D: Appl. Phys. **54**(17), 175105 (2021)

33. C. Ang, A. Bhalla, L. Cross, Phys. Rev. B Condens. Mater. **64**(18), 184104 (2001)

34. C. Ang, Z. Yu, Phys. Rev. B Condens. Mater. **69**(17), 174109 (2004)

35. S. Pal, N.S. Das, S. Bhattacharjee, S. Mukhopadhyay, K.K. Chattopadhyay, Mater. Res. Express **6**(10), 105029 (2019)

36. S. Yadav, M. Chandra, K. Singh, AIP Conf. Proc. **1953**(1), 050074 (2018)

37. H. Zheng, G.C. de Györgyfalva, R. Quimby et al., J. Eur. Ceram. Soc. **23**(14), 2653–2659 (2003)

38. A.A. Kholodkova, M.N. Danchevskaya, Y.D. Ivakin, G.P. Muravieva, A.S. Tyablikov, J. Supercrit. Fluids **117**, 194–202 (2016)

39. J. Parsons, L. Rimai, Solid State Commun. **5**(5), 423–427 (1967)

40. C. Koops, Phys. Rev. **83**(1), 121 (1951)

41. P. Sengupta, P. Sadhukhan, A. Ray, R. Ray, S. Bhattacharyya, S. Das, J. Appl. Phys. **127**(20), 204103 (2020)

42. S. Bhattacharjee, A. Banerjee, N. Mazumder, K. Chanda, S. Sarkar, K.K. Chattopadhyay, Nanoscale **12**(3), 1528–1540 (2020)

43. S. Bhattacharjee, N. Mazumder, S. Mondal, K. Panigrahi, A. Banerjee, D. Das, S. Sarkar, D. Roy, K.K. Chattopadhyay, Dalton Trans. **49**(23), 7872–7890 (2020)

44. R. De Souza, E. Dickey, Philos. Trans. Royal Soc. A **377**(2152), 20180430 (2019)

45. S. Bhattacharjee, S. Mondal, A. Banerjee, K.K. Chattopadhyay, Mater. Res. Express **7**(4), 044001 (2020)

46. N. Rezlescu, E. Rezlescu, Phys. Status Solidi A **23**(2), 575–582 (1974)

47. R.-A. Eichel, Phys. Chem. Chem. Phys. **13**(2), 368–384 (2011)

48. M.M. Bhunia, K. Panigrahi, C.B. Naskar, S. Bhattacharjee, K.K. Chattopadhyay, P. Chattopadhyay, J. Mol. Liq. **325**, 115000 (2021)

49. A.K. Jonscher, Nature **267**(5613), 673–679 (1977)

50. K. Funke, Solid State Ionics **28**, 100–107 (1988)

51. K. Funke, Prog. Solid State Chem. **22**(2), 111–195 (1993)

52. M. Sindhu, N. Ahlawat, S. Sanghi, A. Agarwal, R. Dahiya, N. Ahlawat, Curr. Appl. Phys. **12**(6), 1429–1435 (2012)

53. J. Liu, Q. Liu, Z. Nie, S. Nie, D. Lu, P. Zhu, Ceram. Int. **45**(8), 10334–10341 (2019)

54. T. Ghosh, A. Bhunia, S. Pradhan, S. Sarkar, J. Mater. Sci.: Mater. Electron. **31**(18), 15919–15930 (2020)

55. R. Bergman, J. Appl. Phys. **88**(3), 1356–1365 (2000)

Authors and Affiliations

Souvik Bhattacharjee[1] 🔵 · **Ratna Sarkar**[1] 🔵 · **Pratik Chattopadhyay**[2] · **Anibrata Banerjee**[2] · **Nirmalya Sankar Das**[3] · **Dimitra Das**[2] · **Kalyan Kumar Chattopadhyay**[1,2] 🔵

✉ Kalyan Kumar Chattopadhyay
kalyan_chattopadhyay@yahoo.com

1 Department of Physics, Jadavpur University, Kolkata 700 032, India

2 School of Materials Science and Nanotechnology, Jadavpur University, Kolkata 700 032, India

3 Department of Physics, Techno International–Batanagar, Kolkata 700 141, India